

Weighted Monte Carlo augmented spherical Fourier-Bessel convolutional layers for 3D abdominal organ segmentation

Wenzhao Zhao¹, Steffen Albert², Barbara D. Wichtmann³, Angelika Maurer³, Ulrike Attenberger³, Frank G. Zöllner², and Jürgen Hesser⁴

¹ Interdisciplinary Center for Scientific Computing, Mannheim Institute for Intelligent Systems in Medicine, Medical Faculty Mannheim, Heidelberg University
wenzhao.zhao@medma.uni-heidelberg.de

² Computer Assisted Clinical Medicine, Mannheim Institute for Intelligent Systems in Medicine, Medical Faculty Mannheim, Heidelberg University

³ Department of Diagnostic and Interventional Radiology, University Hospital Bonn

⁴ Interdisciplinary Center for Scientific Computing, Central Institute for Computer Engineering, CSZ Heidelberg Center for Model-Based AI, Data Analysis and Modeling in Medicine, Mannheim Institute for Intelligent Systems in Medicine, Medical Faculty Mannheim, Heidelberg University.

Abstract. Filter-decomposition-based group equivariant convolutional neural networks show promising stability and data efficiency for 3D image feature extraction. However, the existing filter-decomposition-based 3D group equivariant neural networks rely on parameter-sharing designs and are mostly limited to rotation transformation groups, where the chosen spherical harmonic filter bases consider only angular orthogonality. These limitations hamper its application to deep neural network architectures for medical image segmentation. To address these issues, this paper describes a non-parameter-sharing affine group equivariant neural network for 3D medical image segmentation based on an adaptive aggregation of Monte Carlo augmented spherical Fourier Bessel filter bases. The efficiency and flexibility of the adopted non-parameter-sharing strategy enable for the first time an efficient implementation of 3D affine group equivariant convolutional neural networks for volumetric data. The introduced spherical Bessel Fourier filter basis combines both angular and radial orthogonality for better feature extraction. The 3D image segmentation experiments on two abdominal medical image sets, BTCV and the NIH Pancreas datasets, show that the proposed methods excel the state-of-the-art 3D neural networks with high training stability and data efficiency. The code will be available at <https://github.com/ZhaoWenzhao/WMCSFB>.

Keywords: 3D affine group equivariant neural networks · spherical Fourier-Bessel bases · medical image segmentation.

1 Introduction

Three-dimensional convolutional neural networks (3D CNNs) have become a popular neural network method for 3D image segmentation[8]. However, 3D CNNs

are limited to local receptive fields. Large convolutional kernel is helpful to help CNNs gain a larger receptive field but is typically difficult to train.

Geometric prior such as geometric transformation invariance or equivariance[3,5] is promising to help stabilize large convolutional kernels and avoid performance saturation on limited medical data. Medical images are rich in local structures, which typically undergo various geometric transformations (typically from the affine transformation group). Therefore, a well-trained deep-learning model must maintain equivariance or invariance to these transformations of local structures[13]. To boost the equivariance of deep learning models, we can investigate two aspects of developing a neural network model: the data and neural network architecture. From the data perspective, it is common to employ data augmentation methods for boosting neural networks’ equivariance performance[20,14]. However, its performance on unseen data is not guaranteed theoretically.

This work aims at developing efficient 3D transformation group equivariant convolutional neural networks (G-CNNs) from the microarchitecture design perspective. More specifically, we focus on 3D filter-decomposition-based group equivariance CNN layers for 3D medical images. It should be noted that there has been a lot of research work on designing rotation equivariant networks specifically for 3D point clouds data[19,25,24,18], which may not be suitable for volumetric medical images. The first 3D group equivariant CNN for volumetric data is proposed in [21] for 3D rotation group equivariance and is based on filter decomposition. This work is summarized in [4] to have a generally applicable method for rotation equivariant CNNs of arbitrary CNNs. After that, there have been few research works for continuing developing filter-decomposition-based 3D group equivariant CNN for 3D medical images. The existing 3D G-CNNs in this aspect rely on parameter-sharing and build computationally expensive convolutional units for good performance, which limits its application to deep CNN architectures. In addition, they are limited to rotation equivariant CNNs and mostly use simple spherical harmonic bases as filter bases, which only parameterize filters supported on a compact ball to represent angular coordinates but lack radial orthogonality.

In this work, we propose an efficient non-parameter-sharing 3D affine group equivariant CNN. Specifically, our contributions are embodied in three aspects:

- We propose an efficient 3D affine group equivariant neural network for volumetric image data for the first time, which is based on a decomposition of the 3D transformation matrix, and is implemented efficiently using the strategy of weighted Monte Carlo G-CNNs. The proposed convolutional layer shows superior affine group equivariance to the state-of-the-art 3D G-CNNs.
- Instead of the basis with only angular orthogonality, we introduce a more expressive basis by combining angular orthogonality and radial orthogonality that lead to the spherical Fourier-Bessel basis to improve the performance of the 3D group equivariant neural networks.
- We demonstrate the use of the proposed methods to improve the training stability and data efficiency of the state-of-the-art 3D deep CNNs in 3D abdominal medical image segmentation tasks.

In the following parts of this paper, we detail our methods in the section of Methods and show the experiments and discussions in the Experiments section. The paper is summarized in the Conclusion section.

2 Methods

2.1 Group and group equivariance

This work considers 3D positive general linear group $GL^+(3, \mathbb{R})$ and its subgroups. $GL^+(3, \mathbb{R})$ corresponds to 3D linear transformations preserving orientation, lines, and parallelism of the 3D space. We consider the 3D transformation matrix $M(a)$ for any subgroup of $GL^+(3, \mathbb{R})$ with $a \in \mathbb{R}^d$ and d the number of parameters for composing the transformation matrix. $M(a)$ can be any simple 3D transformation ($d = 1$). A simple 3D transformation means that its corresponding transformation matrix has only one parameter or variable.

We can also construct a $M(a)$ via matrix decomposition, i.e., a series of multiplication of simple transformation matrices, for example,

$$\begin{aligned} M(a) = & R_1(\theta_1)R_3(\theta_3) \cdot \\ & A_1(\alpha)A_2(\beta)A_3(\gamma) \cdot \\ & S_{20}(s_{20})S_{10}(s_{10})S_{21}(s_{21})S_{01}(s_{01}) \cdot \\ & S_{12}(s_{12})S_{02}(s_{02}) \end{aligned} \quad (1)$$

where we have $a = (\theta_1, \theta_3, \alpha, \beta, \gamma, s_{01}, s_{10}, s_{02}, s_{20}, s_{12}, s_{21}) \in \mathbb{R}^{11}$ a parameter vector for transformations. R_n , A_n , and S_{mn} represent the simple rotation along n -th dimension, the simple scaling along the n -th dimension, and the simple shear transformation from the m -th dimension to the n -th dimension, respectively.

We have the following theorem for the above construction:

Theorem 1. *Any element in $GL^+(3, \mathbb{R})$ can be decomposed into the form of (1). Any 3×3 matrix constructed via (1) belongs to $GL^+(3, \mathbb{R})$.*

The proof for this theorem is obvious. This theorem shows that such decomposition builds up the $GL^+(3, \mathbb{R})$ group.

A 3D affine group G is constructed by a semidirect product between the space vector \mathbb{R}^3 and the general linear group. An affine group element $g \in G$ can be written as $g = (x, M(a))$ with $x \in \mathbb{R}^3$ the spatial position. For any group element g_1 and g_2 , the group product is defined as

$$\begin{aligned} g_1 \cdot g_2 = & (x_1, M(a_1)) \cdot (x_2, M(a_2)) \\ = & (x_2 + M(a_1)x_1, M(a_1)M(a_2)) \end{aligned} \quad (2)$$

In this paper, the group we considered is assumed to be locally compact.

Applying a group transformation to an index set \mathcal{X} leads to a group action $T : G \times \mathcal{X}$. The group product with respect to group action satisfies

$$T(g_1 \cdot g_2, x) = T(g_1, T(g_2, x)) \quad (3)$$

For applying a group transformation to a function space $L_V(\mathcal{X}) : \{f : \mathcal{X} \rightarrow V\}$, we have group action \mathbb{T}_g defined accordingly as $\mathbb{T}_g : f \rightarrow f'$ where $f'(T(g, x)) = f(x)$.

A group equivariance mapping $\phi : L_{V_1}(\mathcal{X}_1) \rightarrow L_{V_2}(\mathcal{X}_2)$ satisfies

$$\forall g \in G, \phi(\mathbb{T}_g(f)) = \mathbb{T}'_g(\phi(f)) \quad (4)$$

where \mathbb{T}_g and \mathbb{T}'_g represents the group action on function f and f' , respectively.

2.2 Group convolution

According to [9], we have

Theorem 2. *A feed-forward neural network is equivariant to the action of a compact group G on its inputs if and only if each layer of the network implements a generalized form of convolution derived from the equation below*

$$(\psi * f)(g) = \int_G \psi(g^{-1} \cdot g') f(g') d\mu(g') \quad (5)$$

where $*$ is the convolution symbol, μ is the Haar measure, and $f, \psi : G \rightarrow \mathbb{C}$.

The convolution defined by (5) is thereby called group convolution.

2.3 Weighted Monte Carlo group convolutional network

This work adopts the weight Monte Carlo G-CNN (WMCG-CNN) strategy as in [23], which can be considered as a "preconditioning" to allow the neural network to have a good group equivariance at the starting point of the training with randomly initialized trainable weights w . Specifically, given $g = (x, M(a))$ and $g' = (u, M(b))$, weighted Monte Carlo group convolution considers weighted group convolution integration on $\mathbb{R} \times G$:

$$\begin{aligned} f^{(l+1)}(g) \\ = \int_{\mathbb{R} \times G} w \cdot \psi(g^{-1} \cdot g') f^{(l)}(g') d\mu(g') d\mu_w(w) \end{aligned} \quad (6)$$

where $f^{(l)}$ denotes the feature map of the l -th layer, and ψ denotes the convolutional filter basis.

Let $g = (x, M(a))$ and $g' = (u, M(b))$. We have

$$\begin{aligned} f_{dec}^{(l+1)}(x, a) \\ = \int_{\mathbb{R}} \int_{\mathbb{R}^d} \int_{\mathbb{R}^3} w C(b) \psi(-x + M(-a)u, M(-a)M(b)) \\ f^{(l)}(u, b) du db dw \end{aligned} \quad (7)$$

where d the number of variables in the parameter vector a or b . $C(b)$ is the normalization coefficient with respect to the Haar measure $\mu(g')$. For the affine matrix $M(b)$ using scaling transformations, there is $C(b) = 2^{-2\alpha_b - 2\beta_b - 2\gamma_b}$. It

should be noted that for simplicity, here the constant coefficients, bias terms, and point-wise nonlinearity in neural networks are omitted.

The discretization implementation is based on a Monte Carlo integral approximation. Different from conventional G-CNN, WMCG-CNN eliminates the weight-sharing between feature channels. Specifically, let c_o and c_i be the channel numbers of output and input feature maps, respectively. For each input-output channel pair (c_o, c_i) , we draw randomly a sample of b and a sample of weight w . For each output channel, we have a sample of a . For each sample of a , there are N samples of b . Then we have

$$f_{c_o}^{(l+1)}(x, a_{c_o}) = \sum_{c_i=0}^{N-1} \sum_u w_{c_o, c_i}^{(l)} C(b) \cdot \psi(-x + M(-a_{c_o})u, M(-a_{c_o})M(b_{b_o, c_i})) f_{c_i}^{(l)}(u, b_{c_o, c_i}) \quad (8)$$

By further replacing the weighted ψ function with the weighted sum of multiple filter bases, we finally get the fully fledged WMCG-CNN. Specifically, let $W_{c_o, c_i}^{(l)}(x, M(a)) = \sum_j w_{c_o, c_i, j}^{(l)} \tilde{\psi}_j(x, M(a))$ with j the basis number and $\tilde{\psi}$ the j -th basis. We can rewrite (8) as

$$f_{c_o}^{(l+1)}(x, a_{c_o}) = \sum_{c_i=0}^{N-1} \sum_u C(b) W_{c_o, c_i}^{(l)}(-x + M(-a_{c_o})u, M(-a_{c_o})M(b_{b_o, c_i})) f_{c_i}^{(l)}(u, b_{c_o, c_i}), \quad (9)$$

As suggested in [23], the WMCG-CNN is often followed by scalar convolutional layers ($1 \times 1 \times 1$ convolutional kernel for 3D CNNs) to boost its equivariance performance.

By pre-calculating the weights, in the inference phase, the WMCG-CNNs have the same computational burden as the standard CNN when using the same kernel size. During the training phase, there is only a tiny increase in computational burden due to the weighted sum of filter bases.

2.4 Spherical Fourier-Bessel basis

Considering a spherical coordinate, the existing works on SE(3) G-CNN[21,4] for volumetric data use the following filter bases

$$\phi_{lmn}(\mathbf{r}) = \Phi(r - n) Y_{lm}(\theta, \phi) \quad (10)$$

where $\mathbf{r} = (r, \theta, \phi)$, Gaussian function $\Phi(r - n) = \exp(-\frac{1}{2}(r - n)^2/\sigma^2)$, and $Y_{lm}(\theta, \phi)$ is the spherical harmonics.

It is clear that the spherical harmonics satisfy angular orthogonality, which means

$$\int_0^{2\pi} \int_0^\pi Y_{l_1, m_1}(\theta, \phi) Y_{l_2, m_2}^*(\theta, \phi) \sin(\theta) d\theta d\phi = \delta_{m_1, m_2} \delta_{l_1, l_2} \quad (11)$$

where δ is Kronecker delta symbol.

However, the radial part $\Phi(r - n)$ lacks orthogonality. It is believed that the orthogonality of bases allows a compact "good" representation of local features by using a small number of bases[22]. To enhance the orthogonality of the radial

part, following [2,6], we replace the Gaussian radial function with the spherical Bessel function to have

$$\phi_{lmn}(\mathbf{r}) = j_l(k_n r) Y_{lm}(\theta, \phi) \quad (12)$$

where $j_l(\cdot)$ is the spherical Bessel function. The index k_n denotes the discrete spectrum of radial modes. As in [6], the value of k_n satisfies the continuous boundary condition by setting $j_{l-1}(k_n R) = 0$ for all l with R the maximal radial of the kernel coordinate.

The Bessel function satisfies orthogonality

$$\int_0^R r^2 j_l(k_n r) j_l(k_{n'} r) dr = \delta_{n,n'} \frac{R^3}{2} [j_l(k_n R)]^2 \quad (13)$$

3 Experiments

3.1 Datasets and experimental setup

We validate our method on two abdominal medical image datasets: BTCV (Beyond-the-Cranial-Vault)[10] and the NIH Pancreas dataset[15]. The details about the datasets and training setup are described in the supplementary material. All the tested networks are implemented with PyTorch. The training is performed on a GPU server with 8 A100 GPUs.

3.2 Ablation experiments

The ablation experiments are performed on BTCV dataset. To save time, the number of training epochs is set to 200. The mean Dice Similarity Coefficient (DSC, %)[17] of five-fold cross validation (CV) is reported. For implementation of our methods, we adopt the filter decomposition as equation (1). We choose MedNeXt-S-k5 from [16] as a base model to build a corresponding WMCG-CNN model. The default setting of the WMCG-CNN model is denoted as "MedNeXt-S-WMCG-sFB-k5-nb27-shear0.25 π ", where the spherical Fourier-Bessel bases are augmented with uniformly random circular shift, random rotation, random shear transformation with shear angle in the range of $[-0.25\pi, 0.25\pi)$, random scaling in the range of $[1, 2)$. The scaling coefficients for the three directions are of the same value, while other augmentation parameters are all independently sampled. To justify the effectiveness of the default setting, we test the cases of not using basis shift, using various ranges of shear angle, using only the spherical harmonics[21,4], and using kernel reparameterization[12].

The suffixes in the model names are used to denote the models of different settings. "kn" means the filter size of $n \times n \times n$. "nbn" means the first n low-frequency bases used per filter. "sph" means the spherical Harmonic bases. "sFB" means the spherical Fourier-Bessel bases. "noshift" means no random circular shift bases. "diffscale" means the scaling coefficients for three directions are sampled independently. "REP" means the kernel reparameterization methods from [12].

The results are shown in Table 1. In addition to DSC, the current and following experimental sections also report the number of trainable parameters in million (10^6), Params(M); the number of Multiply–Accumulate Operations in giga (10^9), MACs(G); Significance of Difference, SD, the p-value of Paired Wilcoxon signed-rank test on comparison with the target methods (marked with the star symbol "*").

Table 1. Ablation experimental results on the BTCV dataset.

Models	Params (M)	MAE (G)	DSC (%)	SD
MedNeXt-S-k5-WMCG-sFB-nb27-noshift	5.56	141.94	81.98±8.80	0.714 ^(*)
MedNeXt-S-k5-WMCG-sFB-nb27-shear0.0	5.56	141.94	81.74±8.38	0.239 ^(*)
MedNeXt-S-WMCG-sFB-k5-nb27-shear0.25 π	5.56	141.94	82.00±8.15	*
MedNeXt-S-WMCG-sFB-k5-nb27-shear0.40 π	5.56	141.94	81.56±8.48	0.049 ^(*)
MedNeXt-S-WMCG-sFB-k5-nb27-diffscale	5.56	141.94	81.60±8.52	0.140 ^(*)
MedNeXt-S-WMCG-sph-k5-nb27-shear0.25 π	5.56	141.94	81.69±9.08	0.496 ^(*)
MedNeXt-S-k5-REP	5.99	141.94	ERR	

3.3 Results with different neural network architectures on abdominal organ segmentation datasets

We test the proposed methods to improve the performance of the state-of-the-art network architectures including nnUNet[8] MedNeXt[16], D-LKA Net[1], UNETR[7], UNETR++[17], UXNet[11], and RepUXNet[12].

The experimental results are shown in Table 2 and Table 3. In the names of the tested models, SE(3) means the SE(3) group convolutional layer from [21]. In the results, "ERR" means that training loss "not a number" error occurred in the training with both the default learning rate and the ten times smaller learning rate. The construction of the networks based on the baseline networks are detailed in the supplementary material.

We also display the mean group-equivariant error (mGE) in Fig. 1 in the supplementary material for the first hidden convolutional layers in the training of the first 60 epochs on the BTCV dataset. The mGE is defined as $mGE = \mathbb{E}(\|\phi(\mathbb{T}_g(f)) - \mathbb{T}'_g(\phi(f))\|)$. For calculation, for each input image, a randomly generated affine transformation $g \in G$ is used with the shear range $[-0.0625\pi, 0.0625\pi)$, the scaling range $[1.0, 1.1)$ and rotation angle range $[-0.125\pi, 0.125\pi)$. It is shown that our method gives the smallest mGE, which allow the neural network to have a faster convergence from the beginning of the training.

Table 2. Results on the BTCV dataset.

Models	Params (M)	MAE (G)	DSC (%)	SD
mnUNet[8]	16.46	186.57	83.00±8.82	0.018 ^(**)
UNETR[7]	92.95	149.08	71.16±10.80	<0.001 ^(**)
UNETR++[17]	42.97	77.30	81.06±7.95	<0.001 ^(**)
UXNET[11]	53.01	1159.10	79.38±8.67	<0.001 ^(**)
RepUXNet[12]	65.83	1410.37	ERR	
MedNeXt-S-k3[16]	5.56	109.66	82.89±8.10	0.131 ^(*)
MedNeXt-S-k5[16]	5.99	141.94	82.53±8.42	0.002 ^(*)
MedNeXt-S-k5+SE(3)	5.63	141.94	82.48±7.80	0.002 ^(*)
MedNeXt-S-k5+WMCG-sFB-nb27	5.56	141.94	83.10±8.20	*
MedNeXt-L-k3[16]	61.79	419.46	83.44±8.07	0.259 ^(**)
MedNeXt-L-k5[16]	63.01	473.73	ERR	
MedNeXt-L-k5+SE(3)	61.62	473.73	82.91±8.30	<0.001 ^(**)
MedNeXt-L-k5+WMCG-sFB-nb27	63.01	473.73	83.56±8.05	**
MedNeXt-L-k5+upkern-retrain[16]	63.01	473.73	83.59±8.08	0.820 ^(***)
MedNeXt-L-k5+WMCG-sFB-nb125-bases_ext	63.01	473.73	83.61±8.07	***

Table 3. Results on the NIH Pancreas dataset.

Models	Params (M)	MAE (G)	DSC (%)	SD
UNETR[7]	92.45	63.53	78.35±9.48	<0.001 ^(***)
UNETR++[17]	42.95	44.17	79.30±9.89	<0.001 ^(***)
UXNET[11]	53.01	579.04	83.37±5.56	0.048 ^(***)
D-LKA Net[1]	62.07	166.63	80.46±8.85	0.005 ^(*)
D-LKA Net+SE(3)	61.67	167.87	81.85±7.38	0.174 ^(*)
D-LKA Net+WMCG-sFB	62.39	167.87	82.42±6.50	*
MedNeXt-L-k3[16]	61.78	209.44	82.98±5.40	0.273 ^(**)
MedNeXt-L-k5[16]	62.99	236.57	82.92±5.89	0.351 ^(**)
MedNeXt-L-k5+upkern-retrain[16]	62.99	236.57	83.12±6.24	0.689 ^(**)
MedNeXt-L-k5+SE(3)	61.62	236.57	81.40±6.86	<0.001 ^(**)
MedNeXt-L-k5+WMCG-sFB	62.99	236.57	83.29±5.21	**
RepUXNet[12]	65.83	704.68	83.71±4.56	0.237 ^(***)
RepUXNet+SE(3)	47.24	679.04	82.06±5.57	<0.001 ^(***)
RepUXNet+WMCG-sFB	50.51	679.04	84.01±5.24	***

4 Conclusion

In this work, we propose an efficient non-parameter-sharing 3D affine G-CNN for the first time, which is implemented by weighted aggregation of Monte Carlo augmented spherical Fourier-Bessel bases. The proposed neural network layer is superior to the state-of-the-art 3D G-CNN layer in affine group equivariance on the volumetric medical image data. The proposed methods consistently improve the performance of the state-of-the-art 3D segmentation neural networks on the small-scale medical image datasets with high training stability and data efficiency. However, it should be noted that the proposed methods are not good at dealing with extremely large kernels such as $21 \times 21 \times 21$, where an extremely large number of filter bases are needed and can bring a huge memory burden to the GPU machine during training. How to mitigate this problem will be studied in future work.

References

1. Azad, R., Niggemeier, L., Hüttemann, M., Kazerouni, A., Aghdam, E.K., Velichko, Y., Bagci, U., Merhof, D.: Beyond self-attention: Deformable large kernel attention for medical image segmentation. In: Proceedings of the IEEE/CVF Winter Conference on Applications of Computer Vision. pp. 1287–1297 (2024)
2. Binney, J., Quinn, T.: Gaussian random fields in spherical coordinates. *Monthly Notices of the Royal Astronomical Society* **249**(4), 678–683 (1991)
3. Bronstein, M.M., Bruna, J., Cohen, T., Velicković, P.: Geometric deep learning: Grids, groups, graphs, geodesics, and gauges. arXiv preprint arXiv:2104.13478 (2021)
4. Cesa, G., Lang, L., Weiler, M.: A program to build e (n)-equivariant steerable cnns. In: International Conference on Learning Representations (2021)
5. Cohen, T.S., Welling, M.: Steerable cnns. arXiv preprint arXiv:1612.08498 (2016)
6. Fisher, K.B., Lahav, O., Hoffman, Y., Lynden-Bell, D., Zaroubi, S.: Wiener reconstruction of density, velocity and potential fields from all-sky galaxy redshift surveys. *Monthly Notices of the Royal Astronomical Society* **272**(4), 885–908 (1995)
7. Hatamizadeh, A., Tang, Y., Nath, V., Yang, D., Myronenko, A., Landman, B., Roth, H.R., Xu, D.: Unetr: Transformers for 3d medical image segmentation. In: Proceedings of the IEEE/CVF winter conference on applications of computer vision. pp. 574–584 (2022)
8. Isensee, F., Jaeger, P.F., Kohl, S.A., Petersen, J., Maier-Hein, K.H.: nnu-net: a self-configuring method for deep learning-based biomedical image segmentation. *Nature methods* **18**(2), 203–211 (2021)
9. Kondor, R., Trivedi, S.: On the generalization of equivariance and convolution in neural networks to the action of compact groups. In: International Conference on Machine Learning. pp. 2747–2755. PMLR (2018)
10. Landman, B., Xu, Z., Igelsias, J., Styner, M., Langerak, T., Klein, A.: Miccai multi-atlas labeling beyond the cranial vault—workshop and challenge. In: Proc. MICCAI Multi-Atlas Labeling Beyond Cranial Vault—Workshop Challenge. vol. 5, p. 12 (2015)
11. Lee, H.H., Bao, S., Huo, Y., Landman, B.A.: 3d ux-net: A large kernel volumetric convnet modernizing hierarchical transformer for medical image segmentation. arXiv preprint arXiv:2209.15076 (2022)

12. Lee, H.H., Liu, Q., Bao, S., Yang, Q., Yu, X., Cai, L.Y., Li, T.Z., Huo, Y., Koutsoukos, X., Landman, B.A.: Scaling up 3d kernels with bayesian frequency re-parameterization for medical image segmentation. In: International Conference on Medical Image Computing and Computer-Assisted Intervention. pp. 632–641. Springer (2023)
13. Lenc, K., Vedaldi, A.: Understanding image representations by measuring their equivariance and equivalence. In: Proceedings of the IEEE conference on computer vision and pattern recognition. pp. 991–999 (2015)
14. Quiroga, F., Ronchetti, F., Lanzarini, L., Bariviera, A.F.: Revisiting data augmentation for rotational invariance in convolutional neural networks. In: Modelling and Simulation in Management Sciences: Proceedings of the International Conference on Modelling and Simulation in Management Sciences (MS-18). pp. 127–141. Springer (2020)
15. Roth, H.R., Lu, L., Farag, A., Shin, H.C., Liu, J., Turkbey, E.B., Summers, R.M.: Deeporgan: Multi-level deep convolutional networks for automated pancreas segmentation. In: Medical Image Computing and Computer-Assisted Intervention–MICCAI 2015: 18th International Conference, Munich, Germany, October 5–9, 2015, Proceedings, Part I 18. pp. 556–564. Springer (2015)
16. Roy, S., Koehler, G., Ulrich, C., Baumgartner, M., Petersen, J., Isensee, F., Jaeger, P.F., Maier-Hein, K.H.: Mednext: transformer-driven scaling of convnets for medical image segmentation. In: International Conference on Medical Image Computing and Computer-Assisted Intervention. pp. 405–415. Springer (2023)
17. Shaker, A., Maaz, M., Rasheed, H., Khan, S., Yang, M.H., Khan, F.S.: Unetr++: delving into efficient and accurate 3d medical image segmentation. arXiv preprint arXiv:2212.04497 (2022)
18. Shen, W., Wei, Z., Ren, Q., Zhang, B., Huang, S., Fan, J., Zhang, Q.: Rotation-equivariant quaternion neural networks for 3d point cloud processing. *IEEE Transactions on Pattern Analysis and Machine Intelligence* (2024)
19. Thomas, N., Smidt, T., Kearnes, S., Yang, L., Li, L., Kohlhoff, K., Riley, P.: Tensor field networks: Rotation-and translation-equivariant neural networks for 3d point clouds. arXiv preprint arXiv:1802.08219 (2018)
20. Wang, R., Walters, R., Yu, R.: Data augmentation vs. equivariant networks: A theory of generalization on dynamics forecasting. arXiv preprint arXiv:2206.09450 (2022)
21. Weiler, M., Geiger, M., Welling, M., Boomsma, W., Cohen, T.S.: 3d steerable cnns: Learning rotationally equivariant features in volumetric data. *Advances in Neural Information Processing Systems* **31** (2018)
22. Xie, P., Wu, W., Zhu, Y., Xing, E.: Orthogonality-promoting distance metric learning: convex relaxation and theoretical analysis. In: International Conference on Machine Learning. pp. 5403–5412. PMLR (2018)
23. Zhao, W., Wichtmann, B.D., Albert, S., Maurer, A., Zöllner, F.G., Attenberger, U., Hesser, J.: Adaptive aggregation of monte carlo augmented decomposed filters for efficient group-equivariant convolutional neural network. arXiv preprint arXiv:2305.10110 (2023)
24. Zhdanov, M., Hoffmann, N., Cesa, G.: Implicit convolutional kernels for steerable cnns. In: Thirty-seventh Conference on Neural Information Processing Systems (2023)
25. Zhu, M., Ghaffari, M., Clark, W.A., Peng, H.: E2pn: Efficient se (3)-equivariant point network. In: Proceedings of the IEEE/CVF Conference on Computer Vision and Pattern Recognition. pp. 1223–1232 (2023)

5 Supplementary material

5.1 Dataset details

BTCV dataset The BTCV dataset[10] consists of abdominal CT scans of 30 subjects. The CT scans were obtained with contrast enhancement in the portal venous phase. For each scan, 13 organs were annotated with the help of radiologists at Vanderbilt University Medical Center.

In the experiments with BTCV dataset, the default training routine is based on [16]. The input patch size is $48 \times 192 \times 192$. The batch size is 2. Neural networks are trained for 1,000 epochs with AdamW optimizer with an initial learning rate 0.001, and weight decay 0.01. nnUNet[8] is trained with SGD optimizer with an initial learning rate of $1e-2$, momentum 0.99, and weight decay $3e-5$. 5-fold cross-validation (CV) is performed using 80:20 splits of training and testing data. The mean performance is reported.

NIH Pancreas dataset The public NIH Pancreas dataset[15] contains 82 contrast-enhanced abdominal CT volumes obtained by contrast enhanced 3D CT scans (around 70 seconds after intravenous contrast injection in portal-venous) from 53 male and 27 female subjects. In the CT volumes, the pancreas was manually annotated by an experienced radiologist.

In the experiments with NIH Pancreas dataset, following [1], 62 samples are used for training, 20 samples are for testing. The default training routine is based on [1]. The input patch size is $96 \times 96 \times 96$. The batch size is 8. The neural networks are trained for 6,000 iterations with SGD optimizer. The initial learning rate is 0.01, momentum 0.9, and weight decay $1e-4$. Different from previous experiments, the MedNeXt networks are trained without deep supervision.

5.2 The construction of different tested neural networks

MedNeXt-L-k5+SE(3) is constructed by replacing all hidden $5 \times 5 \times 5$ convolutional layers with the corresponding SE(3)[21] G-CNN layers with the same kernel size. MedNeXt-S+WMCG-sFB-k5-nb27 and MedNeXt-L+WMCG-sFB-k5-nb27 are constructed by replacing all hidden $5 \times 5 \times 5$ -kernel convolutional layers with the proposed WMCG spherical Fourier Bessel G-CNN layers of kernel size $5 \times 5 \times 5$ using the first 27 low-frequency bases. "upkern-retrain" is the kernel upscaling retraining method from [16], where the $3 \times 3 \times 3$ kernels from a trained MedNeXt are upscaled to initialize the to-be-trained $5 \times 5 \times 5$ MedNeXt. "bases_ext" is our proposed method for extending the number of bases in the trained WMCG-sFB layers from 27 to 125 in retraining, where the trained 27 bases are reused.

D-LKA Net+SE(3) is constructed by replacing all the $7 \times 7 \times 7$ convolutional layers with the corresponding SE(3) layers followed by a $1 \times 1 \times 1$ convolutional layer. D-LKA Net+WMCG-sFB is constructed by replacing all the $7 \times 7 \times 7$ convolutional layers with the corresponding WMCG-sFB layer followed by a $1 \times 1 \times 1$ convolutional layer.

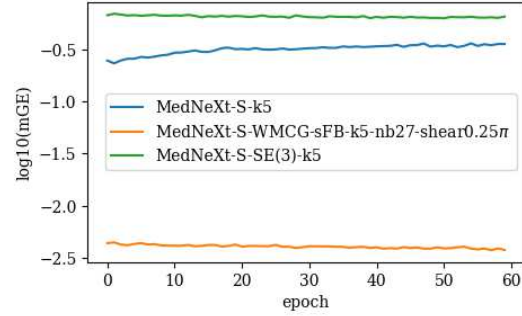


Fig. 1. The mGE of the first hidden convolutional layer of the networks.

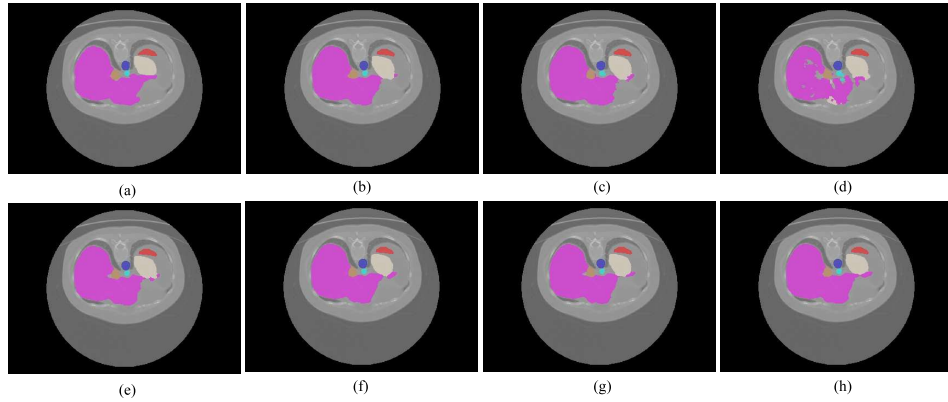


Fig. 2. The segmentation results on BTCV dataset. (a) Ground truth; (b) nnUNet; (c) UNETR++; (d) UXNET; (e) MedNeXt-L-k3; (f) MedNeXt-L-k5+SE(3); (g) MedNeXt-L-k5+upkern-retrain; (h) MedNeXt-L-k5+WMCG-sFB-nb27.

RepUXNet+SE(3) is constructed by replacing all the hidden $3 \times 3 \times 3$ layers with the bottleneck block from MedNeXt, where the first convolutional layer is further replaced with a corresponding SE(3) layer but with the number of channel groups as 8. RepUXNet+WMCG-sFB is built by replacing the SE(3) layer in RepUXNet+SE(3) with a corresponding WMCG-sFB layer.

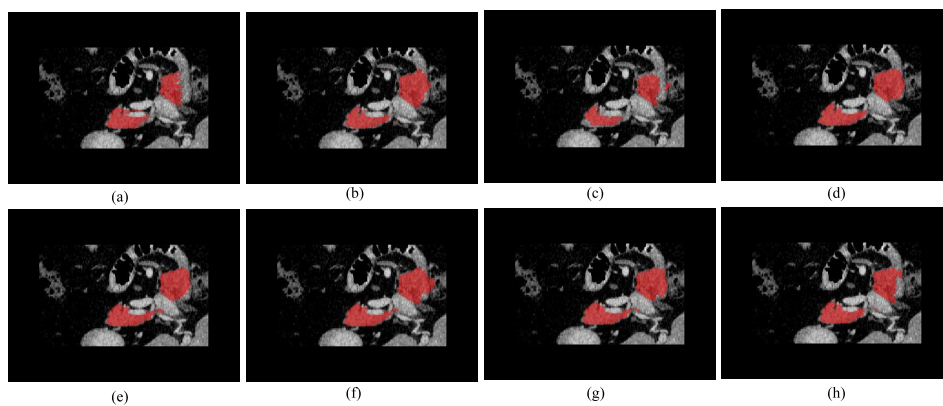


Fig. 3. The segmentation results on NIH Pancreas dataset. (a) Ground truth; (b) UNETR; (c) UNETR++; (d) UXNET; (e) MedNeXt-L-k3; (f) MedNeXt-L-k5+SE(3); (g) MedNeXt-L-k5+upkern-retrain; (h) MedNeXt-L-k5+WMCG-sFB.